ACS NANO

www.acsnano.org

ARTICLE

Dynamic Tuning of Moiré Superlattice Morphology by Laser Modification

Xinyun Wang,[#] Yuzhou Zhao,[#] Xiao Kong,[#] Qi Zhang, Hong Kuan Ng, Sharon Xiaodai Lim, Yue Zheng, Xiao Wu, Kenji Watanabe, Qing-Hua Xu, Takashi Taniguchi, Goki Eda, Kuan Eng Johnson Goh, Song Jin, Kian Ping Loh, Feng Ding,* Wanxin Sun,* and Chorng Haur Sow*

Cite This: *ACS Nano* 2022, 16, 8172–8180

Read Online

ACCESS | Metrics & More | Article Recommendations | Supporting Information

ABSTRACT: **In artificial van der Waals (vdW) layered devices, twisting the stacking angle has emerged as an effective strategy to regulate the electronic phases and optical properties of these systems. Along with the twist registry, the lattice reconstruction arising from vdW interlayer interaction has also inspired significant research interests. The control of twist angles is significantly important because the moiré periodicity determines the electron propagation length on the lattice and the interlayer electron−electron interactions. However, the moiré periodicity is hard to be modified after the device has been fabricated. In this work, we have demonstrated that the moiré periodicity can be precisely modulated with a localized laser annealing technique. This is achieved with regulating the interlayer lattice mismatch by the mismatched lattice constant, which originates from the variable density of sulfur vacancy generated during laser modification. The existence of sulfur vacancy is further verified by excitonic emission energy and lifetime in photoluminescence measurements. Furthermore, we also discover that the mismatched lattice constant has the equivalent contribution as the twist angle for determining the lattice mismatch. Theoretical modeling elaborates the moiré−wavelength-dependent energy variations at the interface and mimics the evolution of moiré morphology.**

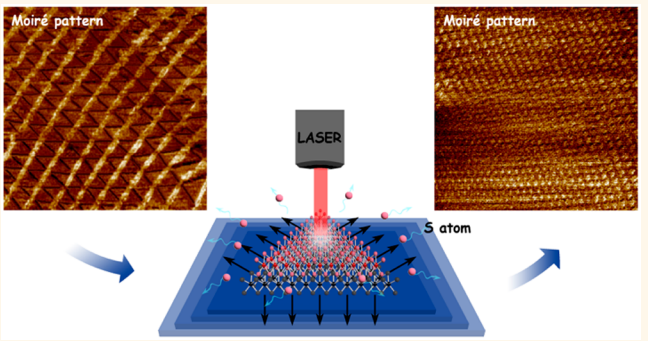

KEYWORDS: *transition metal dichalcogenide, moiré superlattice, laser modification, defects, photoluminescence*

INTRODUCTION

Moiré superlattices generated by a simple twist in van der Waals (vdW) layered crystals have been demonstrated as an effective approach that can dramatically manipulate the electrical and optical properties of the materials.[1−6] Interesting phenomena have been observed in these systems, including strong piezoelectric textures in twisted transition metal dichalcogenides (TMDs),[7,8] flipped electric dipole moments,[9] zero-dimensional quantum emitter,[10] and secondary Dirac bands in twisted bilayer graphene.[11] Considerable progress has also been made in understanding the potential of lattice reconstruction in those twisted systems.[7,11,12] Most prior works focus on the moiré superlattices that are solely controlled by the twist angle. Indeed, the interlayer lattice mismatch is determined by both twist angle and mismatched lattice constant (the difference of the lattice constants between the top and bottom layers). In theory, we can also manipulate moiré superlattices with the mismatched lattice constant. Meanwhile, recent theoretical studies[13,14] and microscopy experiments[10] have also proved that the moiré morphology and the correlated electronic structure can be strongly influenced by external strain. However, there is no systematic or controllable approach to constructing such moiré superlattices in experiments.

In this work, by utilizing the WS_2/WS_2 stacked bilayer as a model system, we employed a scanning laser modification technique to dynamically tune the moiré superlattice morphology. In addition, density functional theory (DFT) calculation is utilized to investigate the effect of mismatched lattice constant on twist structures, where we find that the mismatched lattice constant and twist angle have equivalent contributions to the moiré morphology. We further verify that the mismatched lattice constant is regulated by the density of

Received: February 16, 2022
Accepted: May 11, 2022
Published: May 16, 2022

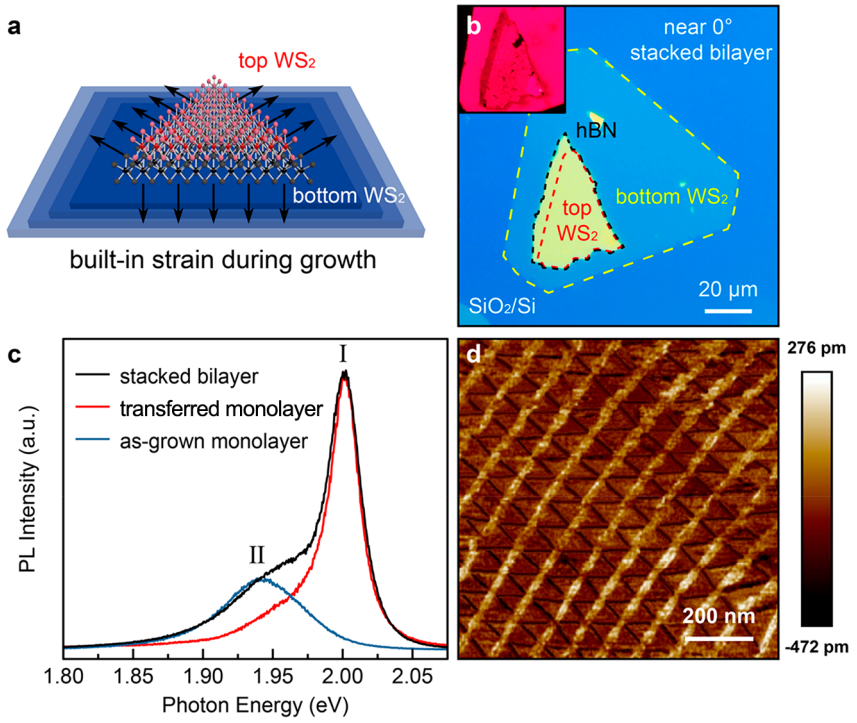

Figure 1. Moiré superlattice in a near 0° WS_2/WS_2 stacked bilayer with strain-engineered lattice mismatch. (a) Schematic of an artificially WS_2 stacked bilayer structure with near 0° twist angle. A built-in tensile strain of bottom WS_2 monolayer is presented due to the mismatch of thermal expansion coefficient between the material and the growth substrate during the chemical vapor deposition growth. (b) Optical microscope image of a near 0° WS_2/WS_2 stacked bilayer with a top hBN capping on a SiO_2/Si substrate. The inset shows the corresponding fluorescence microscope image. (c) Photoluminescence (PL) spectra collected from a stacked bilayer and an as-grown monolayer on SiO_2/Si, as well as transferred monolayer WS_2 flakes. (d) PFM image of the moiré superlattices in the near 0° WS_2/WS_2 stacked bilayer shown in panel b.

sulfur vacancy introduced during laser annealing. Such an intriguing phenomenon is further supported by tracing the photoluminescence (PL) emission energy and lifetime of the corresponding excitons from the WS_2/WS_2 stacked bilayer. Of greater scope, we thus demonstrate that lattice mismatch induced by the lattice constant can be an important factor to reshape the moiré morphology.

RESULTS AND DISCUSSION

We start by fabricating the stacked bilayer devices using a polycarbonate (PC) dry transfer method.[15] We use triangular-shaped chemical vapor deposition (CVD)-grown WS_2 monolayers[16] with sharp terminations, which have random orientations on the growth substrates. During the fabrication process, the WS_2 top layer was first torn and picked up from an individual WS_2 monolayer by hBN and transferred onto the bottom monolayer. Figure 1a shows a typical structure schematic of the WS_2/WS_2 stacked bilayer device on a SiO_2/Si substrate. In contrast to earlier studies, where both layers are mechanically exfoliated from single crystals, the CVD-grown monolayers at the bottom retain a built-in tensile strain caused by mismatched thermal expansion coefficients between the SiO_2/Si substrate and the WS_2 flakes, when cooling from a high growth temperature (around 1000 °C).[16,17] Meanwhile, the built-in tensile strain is released when it is picked up from the substrate. Because of that, despite being the same material, there is a lattice mismatch between the strained bottom layer and the strain-released top layer, forming a moiré superlattice. The interlayer twist angle can be determined by measuring the angle between the edges of the two triangular flakes, which can be directly extracted from the microscope images. This angle-determining method relies on two well-established facts from previous literature: first, most CVD-grown triangular TMD monolayers are verified to be single crystalline across the entire flake; second, the sharp edges of such a triangular TMD monolayer are associated with certain edge orientations.[18−20] Therefore, the orientation of the two flakes can be unambiguously identified. Figure 1b presents an optical microscope image of a near 0° WS_2 stacked bilayer on SiO_2/Si with a hBN crystal top capping (hBN thickness is around 30−50 nm). The top-left inset in Figure 1b shows the corresponding fluorescence microscope image. Interestingly, the fluorescence emission from the stacked bilayer region is slightly more intensified compared to the monolayer region (comparing with both covered under hBN).

We also carried out the photoluminescence (PL) measurement on this stacked bilayer at room temperature, as shown in Figure 1c. The PL spectrum of the stacked bilayer shows two peaks with a notable spectral shift of about 50 meV, where the higher energy peak is denoted as peak I and the lower energy peak is denoted as peak II. We found that the position of peak I always stays in line with the PL peak of the monolayers that are transferred onto hBN, while peak II follows the PL peak position of the CVD-grown monolayers. Such energy variation between the CVD-grown and transferred monolayers can be attributed to the built-in strain in monolayers caused by the growth process, as we discussed above.[21−23] Contrary to the bottom monolayer that is bonded to its growth substrate and under tensile stress, the top layer is released to a relaxed state after being picked up from the growth substrate. Therefore, a

https://doi.org/10.1021/acsnano.2c01625
ACS Nano 2022, 16, 8172−8180

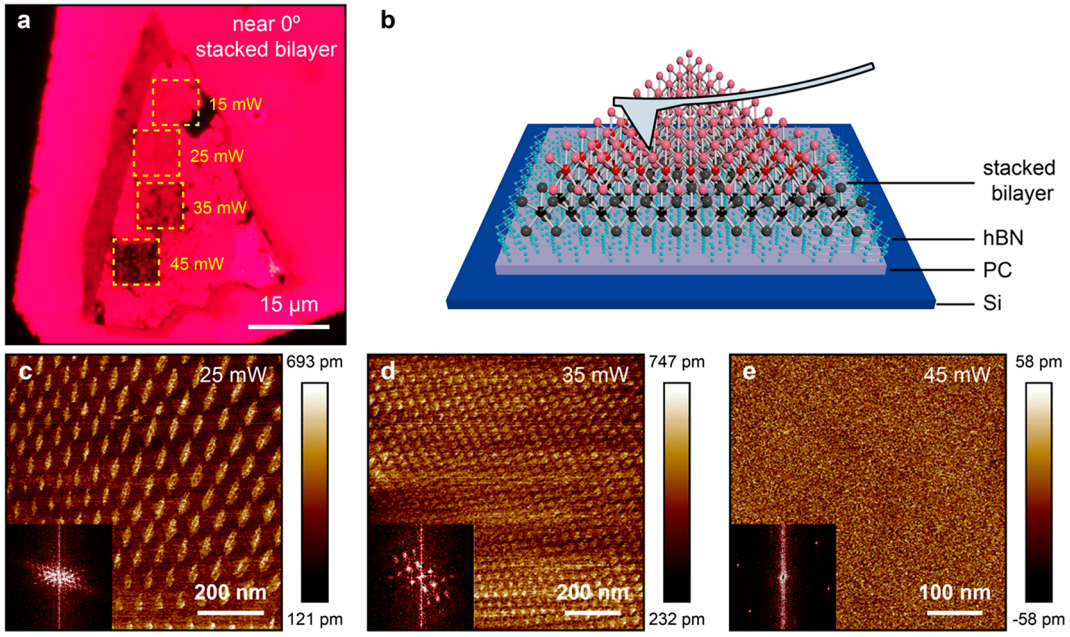

Figure 2. Evolution of reconstructed moiré superlattices in a near 0° WS_2/WS_2 stacked bilayer modulated by localized laser annealing. (a) Fluorescence microscope image of the device after laser modification with different laser powers of 15, 25, 35, and 45 mW, respectively. (b) Schematic of an artificially stacked bilayer investigated by PFM characterization. (c–e) Evolution of the reconstructed moiré superlattice with decreasing moiré wavelength after laser modification, which is revealed by lateral PFM mode with insets of the corresponding FFT images.

strain-induced lattice mismatch is established at the interface of the stacked bilayer during the step of sample fabrication. On the basis of the analysis above, the two PL peaks of the stacked bilayer in Figure 1c can thus be identified as the coexistence of two "independent" intralayer excitons from the relaxed top monolayer and the strained bottom monolayer, according to the previous reports.[24,25] This is further verified with a gate-dependent PL measurement, which shows zero Stark shift (Supporting Information Figure S1).

In TMD moiré superlattices, the localized lattice mismatch will generate a spatially inhomogeneous electromechanical response induced by an AC electric field, which can be used for imaging the moiré patterns using piezoresponse force microscopy (PFM) at the nanoscale.[26] The stacked bilayer flake on SiO_2/Si was first spin-coated with a PC film and then peeled off from the growth substrate. Next, the entire stack was flipped and transferred to a highly doped Si substrate for PFM scanning. Figure 1d shows that a triangular moiré pattern can be clearly observed in the PFM amplitude channel, which is also distinguished from the rigid-lattice moiré superlattice that is hexagonal shaped. The domain wall array shows a large electromechanical response driven by the piezoelectric effect, indicating a non-centrosymmetric stacking order, whereas the electromechanical response of the domain regions is much weaker, suggesting a centrosymmetric stacking order in central regions. The sharp contrast between the domain walls and central regions illuminates a lattice reconstruction in the stacked bilayer.[11,26,27]

By micropatterning the sample with a scanning focused laser beam, the laser modification technique has been demonstrated as a precise local annealing tool.[28,29] We further employed this technique to the WS_2 stacked bilayer system and attempted to manipulate moiré morphology (details can be found in Methods). We selected four regions in the stacked bilayer for laser scanning with increasing laser power: 15, 25, 35, and 45 mW, respectively. Figure 2a shows a fluorescence microscope image of the stacked bilayer after laser modification, where the modified regions are marked by yellow dashed rectangles. We find the fluorescence emission progressively decays with increasing laser powers, which indicates the presence of vacancy defects generated by the focused laser beam.[30,31] To rule out the possibility of structural destruction induced by the high-power laser, we carried out laser modifications and followed by transmission electron microscope (TEM) analysis on a WS_2 monolayer, where the sample was scanned inside a vacuum chamber with a pressure of $\sim 10^{-2}$ mbar to avoid oxidation in air.[30] Similar to the sample covered with hBN, a slight reduction of the fluorescence intensity is observed at the high-power-modified domain (Figure S2) and no significant structure destruction is found in the corresponding diffraction images (Figure S3). These results imply that the high-power laser will not destroy the material's structure, while some amount of vacancy defects can be generated during the annealing process.

We then apply PFM to trace the evolution of the moiré superlattices. Figure 2b shows the typical sample stacking configuration for PFM characterization, and the PFM images in Figure 2c–e reveal the moiré pattern evolution after laser modification. The moiré pattern in the 15 mW region is not shown here, as it is hard to distinguish from local distortion (Figure S4). Moreover, the corresponding fast Fourier transforms (FFT, bottom left insets) confirm the 6-fold symmetry of the moiré superlattices and the presence of uniaxial strain from the underlying substrate. Here in Figure 2c, the slightly elongated oval pattern is expected from the uneven distortions during the transfer process.[10] Surprisingly, the moiré wavelength, λ_m, of the superlattice distinctly decreases with increasing laser power and eventually becomes undetectable by PFM. These results are somewhat counter-intuitive, as we initially expect that the laser annealing would

https://doi.org/10.1021/acsnano.2c01625
ACS Nano 2022, 16, 8172–8180

relax the tensile strain in the bottom layer causing it to shrink back to a relaxed lattice, and a decreased mismatched lattice constant should lead to an increasing moiré wavelength. Yet, experimentally we observed decreasing moiré wavelengths. Nevertheless, the overall results still indicate that the moiré morphology, specifically moiré wavelength, can be precisely tuned by laser modification but through a different mechanism. Additionally, to verify the change of the moiré wavelength is not from external strain variations, we fabricated a near 1° twisted WS_2 bilayer by using the monolayers grown on n-doped Si substrates, which can minimize the strain variations and be uninterruptedly scanned by PFM (Figure S5). The result is also consistent with the observations above and thus proves the repeatability of the laser modification method.

Generally, the moiré wavelength is determined by twist angle and mismatched lattice constant between the top and bottom layers (Figure S6). Therefore, to understand how laser modification changes the moiré wavelength, one should consider these two factors as the possible variables during laser annealing. In our experiments, since no rotation of the top monolayer was observed,[32] we can thus exclude the twist angle as the cause of the decrease of moiré wavelength. The trend of moiré pattern evolution also rules out the relaxing of the bottom layer; therefore, it leaves the possibility that the top layer shrinks, causing a larger mismatched lattice constant. Following these considerations, *in situ* PL measurement was employed to explore correlations between the moiré superlattice observed in PFM and the local optical properties, where the mismatch lattice constant at each domain can be read out optically.[17,33,34] As shown in Figure 3a, after the laser modification, the PL intensities of both peak I and peak II decrease with increasing laser powers. However, the two peak positions nearly remain the same, with only peak II of the 45 mW annealing region undergoing a red shift. The observations above indicate the built-in strain of the top and bottom monolayers remains unchanged with laser power between 15 and 35 mW. Furthermore, under high-power excitation of 45 mW, another low-energy peak (denoted as peak III) at around 1.75 eV is discovered, as shown in Figure 3b. Referring to the previous reports,[35−38] peak III is attributed to radiative recombination of bound excitons (X_B), *i.e.*, neutral excitons (X_0) bound to the sulfur vacancy generated during laser modification. We note that the stacked bilayer is blanketed with a hBN crystal during laser modification, where oxidation/doping is suppressed and thus the vacancy defect is most likely to form. Here we primarily consider sulfur vacancy because transition-metal atoms are thermodynamically more stable than chalcogen atoms.[39] Additionally, no blue shift of the emission peak was observed, which excludes the possible contribution from tungsten vacancy.[40] More detailed power-dependent PL spectra can be found in Figure S7, where the peak III intensity increases at higher doses. In addition, we also carried out time-resolved PL measurements to gain further insight into the defect-mediated exciton dynamics. As shown in Figure 3c, a longer exciton lifetime is observed from peak III (200 ps) than peak I and peak II (both with 160 ps), which is due to the slow release of holes from the trap states of defects.[35,41] Therefore, on the basis of the decreased PL intensity and longer exciton lifetime, we have evidence to support the presence of sulfur vacancy generated during laser modification.

To investigate the role of strain-induced lattice mismatch on lattice reconstruction, we also inspected a stacked bilayer with

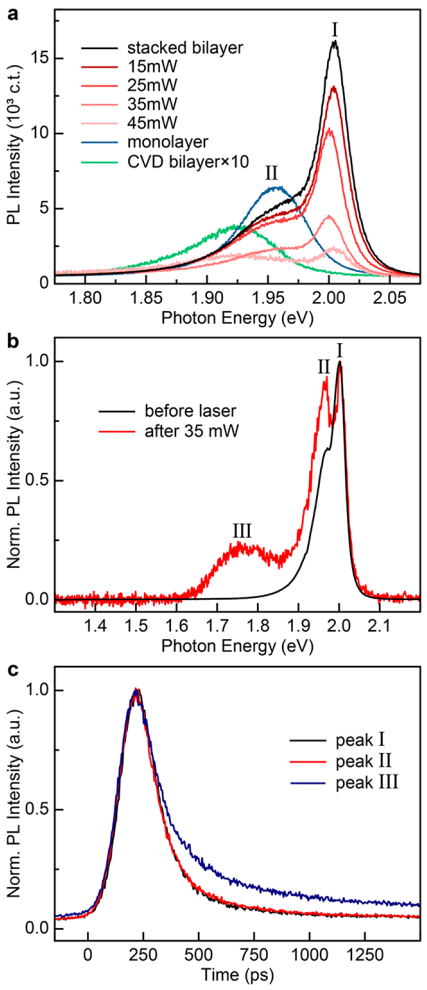

Figure 3. Photoluminescence characterization of the near 0° WS_2/WS_2 stacked bilayer device. (a) PL spectra with different laser power treatments collected from the corresponding regions in Figure 2b. Two direct-band PL peaks arise in the spectra, which are attributed to the intralayer neutral excitons of stacked bilayer under different strains. (b) Normalized PL spectra of the stacked bilayer before (black) and after (red) 35 mW laser modification. (c) Corresponding time-resolved PL spectra of peaks I, II, and III, where the lifetime of peak III is prolonged due to the presence of sulfur vacancy traps that inhibit recombination.

minimal strain difference by using liquid nitrogen to decouple the monolayers from their growth substrates and thus release the built-in tensile strain from growth substrates. Figure S8 shows a clearly quenched fluorescence, and no periodic moiré superlattices are revealed in PFM at such unstrained stacked bilayers. Moreover, during sample fabrication using decoupled monolayers, we found that moiré superlattices are usually difficult to survive with small twist angles. On the basis of the analysis above, we speculate that the strain difference at interfaces does appear as an important precondition for the survival of the twist structure and thus allows more space for manipulating the moiré morphology.

With the discussion above, we now turn to inspect the influence of the density of sulfur vacancy on the moiré wavelength, with the twist angle and the strain unchanged. To reduce complexity, we first investigate the variation of lattice constant in the top monolayer with introduced sulfur vacancy, where the bottom monolayer remains pristine. In this scenario,

https://doi.org/10.1021/acsnano.2c01625
ACS Nano 2022, 16, 8172−8180

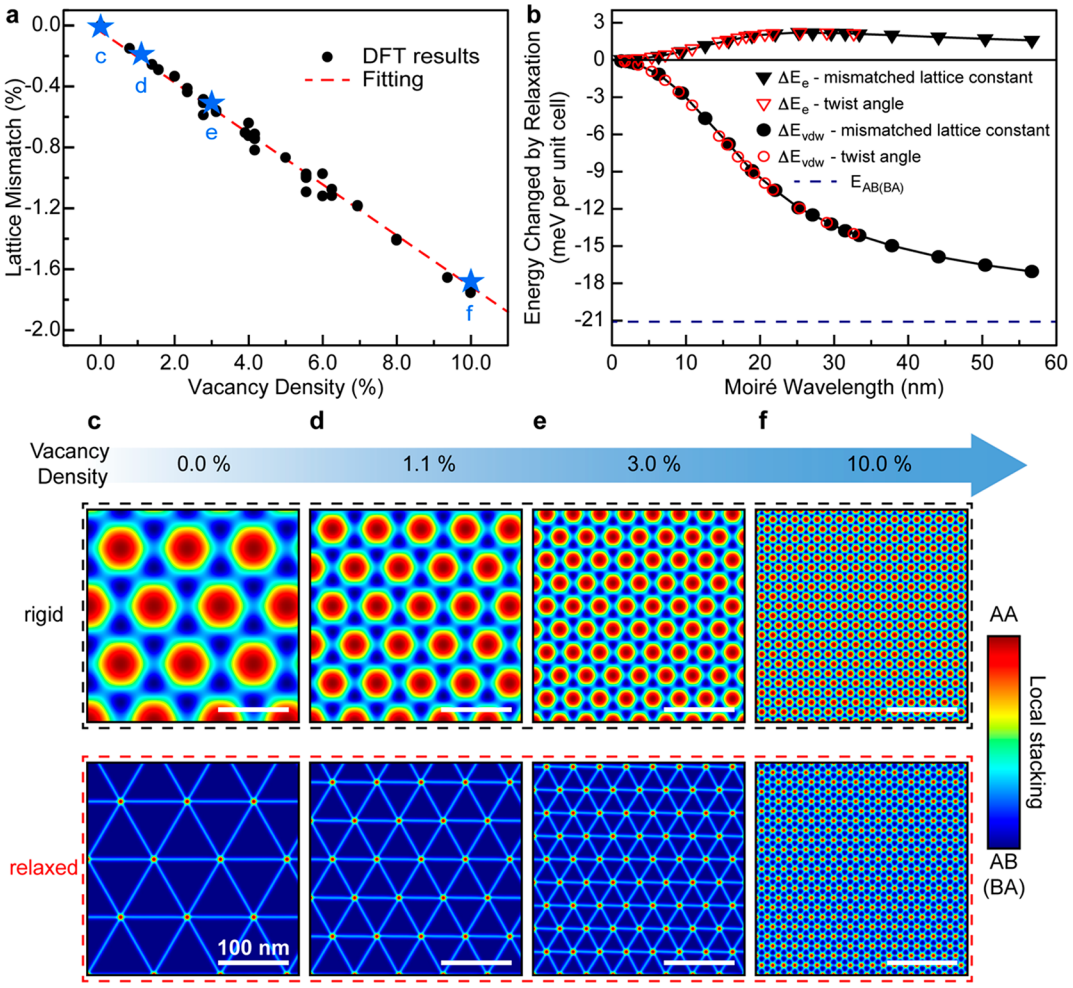

Figure 4. Calculated stacking patterns with various mismatched lattice constants at a 0° twist angle. (a) Evolution of the biaxial lattice mismatch as a function of the density of evaporated sulfur vacancy, where $\rho_S = N_{evap\,S}/N_S$. (b) During the lattice reconstruction process, change of the elastic and the vdW energy only dependent on the moiré superlattices size. We note that the mismatched lattice constant and twist angle both contribute equally to the size of moiré superlattices. (c–f) Transition of stacking configuration before and after lattice reconstruction at various mismatched lattice constants, modeling the impact of sulfur vacancy density relating to different laser powers. The calculated moiré patterns are consistent with our experimental results in Figure 2. All scale bars are 100 nm.

the variation of lattice constant in the top monolayer is thus naturally regarded as the change of biaxial lattice mismatch in the twisted system. Here, density functional theory (DFT) was adapted for calculating, and the detailed calculation models are shown in Methods and Supporting Information. As shown in Figure 4a, the resultant mismatched lattice constant is evaluated as a linear function of the density of sulfur vacancy in the low-density region: $\Delta L/L = -0.167\rho_S$; here, $\Delta L/L$ is the change of lattice constant and ρ_S is the density of sulfur vacancy. Since sulfur vacancy shrinks the lattice constant in the top monolayer while the built-in tensile strain enlarges the lattice constant in the bottom monolayer, the increased sulfur vacancy density is expected to give rise to a smaller moiré wavelength, which corroborates our experimental observations.

Following these considerations, we developed a numerical method to simulate the local stacking configurations of bilayer WS_2 across the moiré supercell. The total energy of this model is defined as $E_t = NE_{WS_2} + E_{elas} + E_{VDW}$, where N is the number of WS_2 per unit cell in one moiré supercell, E_{WS_2} is the energy of the WS_2 monolayer per unit cell, E_{elas} is the overall elastic energy from in-plane bonding within each layer that tends to restore the structure, and E_{VDW} is the overall energy of interfacial vdW interaction that favors low-energy and high-symmetry AB(BA) stacking. More specifically, the elastic energy

$$E_{elas} = \sum \frac{1}{2}E\left[\left(\frac{\partial r_x}{\partial x}\right)^2 + \left(\frac{\partial r_y}{\partial y}\right)^2\right] + G\left(\frac{\partial r_x}{\partial y} + \frac{\partial r_y}{\partial x}\right)^2$$

is calculated by the displacement, $\boldsymbol{r}$, defined on each W atom (Figure S9) and the moduli are fitted from DFT results (Figure S10), where the in-plane strain modulus and shear modulus are E = 225 GPa and G = 92 GPa, respectively. The stacking energies are calculated by the generalized stacking fault energy surface $E_{VDW} = \sum_i E_{GSFE}(u_i,v_i)$, where u_i and v_i are the relative positions of the ith W atom projected to the other layer. The $E_{GSFE}(u_i,v_i)$ are also fitted by the DFT calculations (Methods and Figure S10).

Figure 4b directly demonstrates the relation between the size of the moiré superlattice and the change of elastic energy, ΔE_{elas}, and stacking energy, ΔE_{VDW}, that are attributed from the reconstruction. On the one hand, ΔE_{elas} has a maximum value at a finite moiré wavelength due to the nature of the

https://doi.org/10.1021/acsnano.2c01625
ACS Nano 2022, 16, 8172–8180

reconstruction, where the bilayer tends to form a more stable AB(BA) stacking while extra energy for a shift of unit cell between two layers is required in one moiré supercell. Specifically, the shift of the unit cell is realized by the deformation localized in narrow transition regions (the bright lines in Figure 4c–e). Notably, the widths of the transition regions are nearly a constant at regions of large moiré wavelength, which indicates a decrease of ΔE_{elas} with increasing moiré wavelength. On the other hand, E_{VDW} always prefers a larger area of high-symmetry AB(BA) stacking and keeps decreasing with increasing moiré wavelength. Overall, the reconstruction of the moiré superlattice is determined by the competition/balance between E_{elas} and E_{VDW}. Surprisingly, for both elastic and stacking energies, the curves of contributions from twist angle and mismatched lattice constant are exactly overlapped, which implies their contributions to the lattice reconstruction coincide quite well. Therefore, the percentage of high-symmetry AB(BA) stacking regions in a twist structure after lattice reconstruction only depends on the size of the moiré superlattice, regardless of the moiré wavelength originating from the twist angle or mismatched lattice constant.

Finally, to visualize the evolution of the moiré superlattice regulated by sulfur vacancy after laser modification, we computed the reconstructed moiré patterns of local stacking as a function of the density of sulfur vacancy (Figure 4c–f). The plots of local stacking order are illustrated by its corresponding stacking energy. Because the twist angle of the sample in Figure 1 is near 0°, we focus on the mismatched lattice constant and do not consider the twist angle in the DFT calculations. First, for the pristine stacked bilayers shown in Figure 1, the built-in tensile strain of the bottom monolayer is estimated as 0.32 %, according to the moiré wavelength revealed in Figure 2. After including the intrinsic 0.32 % tensile strain, the total interlayer lattice mismatches turn out to be 0.32, 0.50, and 0.82 % for stacked bilayers with laser powers of 0, 25, and, 35 mW, and the experimental moiré wavelengths are 100, 63, and 40 nm, respectively (Figure 4c–e). Here the sample of 45 mW is not discussed in detail because its moiré wavelength is out of the PFM resolution. The densities of sulfur vacancy generated by 25 and 35 mW laser annealings are expected to be 1.1 and 3.0 %, respectively.

CONCLUSION

In summary, we have explored the pathway to moiré morphology engineering using the scanning laser modification, where the moiré wavelength can be progressively modulated by laser power. Furthermore, we proposed a model for calculating the moiré superlattice and proved that the twist angle and mismatched lattice constant both contribute equally to the size of the moiré patterns. Specifically, we have demonstrated that the mismatched lattice constant is composed of the material's built-in strain and vacancy defects. The latter can be generated during laser annealing, and it is supported with our optical observations. We thus demonstrate that the mismatched lattice constant in a twist system can be an additional degree of freedom to dynamically manipulate the moiré wavelength. Importantly, such a lattice-mismatch-dependent system may be utilized to study strongly correlated quantum many-body physics, where the electronic matter wave is closely related to the moiré wavelength.

METHODS

Sample Preparation. A polycarbonate (PC) dry transfer method[15] was adopted to fabricate artificial twisted bilayer WS_2 devices. First, the CVD-grown monolayers were immersed in liquid nitrogen for around 4 min in order to decouple the flakes from SiO_2/Si substrates. Meanwhile, hBN flakes were mechanically exfoliated onto SiO_2/Si substrates. Two triangular WS_2 monolayers on the same substrate were also selected in advance. On the basis of the single crystallinity across a triangle, the twisting angle between the two layers can be directly measured through an optical microscope. Then, a PC-coated poly(dimethylsiloxane) (PDMS) stamp was lowered to pick up a hBN flake at 100 °C (the hBN flake can also be used to first pick up graphene as a device gate if necessary). Next, this hBN flake was engaged to the first monolayer WS_2 at 120 °C for 15 min for better adhesion. After detachment from the first monolayer, we rotated the substrate to control the twist angle between the two layers. Then this hBN-WS_2 stack was brought into contact with the second monolayer WS_2, forming a bilayer structure with a predetermined twisting angle. The stack can also be transferred to a second hBN flake, which serves as a bottom substrate. For PFM measurements, the TBL device was peeled off by a PC film and then flipped to allow the TBL to face up. The whole stack was placed onto a highly doped Si substrate and heated at 100 °C for 5 min for better adhesion. The accuracy of the twist angle is around 1° using this method.

Photoluminescence Measurement. A WITec alpha300R confocal Raman microscope system equipped with 532 nm laser excitation was used for PL collection under ambient conditions at room temperature. A 100× objective lens was used to focus the laser spot on the sample surface to a diameter of around 1 μm. A spectral grating with 800 lines/mm was used for collecting PL spectra. Gate- and temperature-dependent PL spectra were obtained with a laser scanning confocal microscope (NT-MDT, NTEGRA Spectra) equipped with an Andor iDus CCD camera (401A-BR-DD-600). The wavelength of the laser is 532 nm with a laser power of less than 10 μW. Samples were loaded in a vacuum chamber ($\approx 10^{-5}$ mbar) cooled by liquid nitrogen or helium. Gate and bias voltages were applied by an Agilent B2902 source/measure unit.

Laser Modification. Samples were laser modified under ambient conditions using a home-built scanning focused laser beam system, equipped with a 532 nm diode-pumped solid-state laser and a 100× objective lens, which gave rise to a focused laser spot of around 1 μm. We made use of an upright optical microscope with a side port that allowed a collimated laser beam to enter. Inside the optical microscope, the laser beam was reflected toward the objective lens by a beam splitter. In this work, we fixed the focused laser beam and scanned the sample using a motorized sample stage with a typical scanning rate of around 10 μm/s. The entire laser modification process was captured by a CCD camera, which allowed us to examine the sample and monitor the process in real time.

Piezoresponse Force Microscopy. The PFM mappings were obtained on a Bruker Dimension Icon SPM in piezoresponse-lateral mode under ambient conditions. We used platinum–iridium-coated, electrically conductive tips (SCM-PIT-V2) with a spring constant $k \approx 3$ N/m. The AC bias magnitudes were around 1000 mV, and the resonance frequencies were around 800 kHz. We kept the tip force less than 50 nN during the scans for producing high-quality images.

Device Fabrication. Conventional e-beam lithography technique was applied to fabricate the electrodes on TBL WS_2, followed by the thermal evaporation of 5 nm Cr and 60 nm Au as metal contact. After liftoff in acetone, the fabricated devices were wire bonded onto a chip carrier for gate-dependent PL measurements.

First-Principles Calculation. The DFT results are calculated by the Vienna *ab initio* simulation package. The Perdew–Burke–Ernzerhof parametrization of generalized gradient approximation (GGA) was used for the exchange–correlation function. The projector-augmented wave potentials were used for ion–electron interactions. The DFT-D3 vdW density functional was used for the corrections of the interlayer vdWs interaction. The electronic self-consistency criterion was set to 10^{-5} eV. For geometry relaxation, the

https://doi.org/10.1021/acsnano.2c01625
ACS Nano 2022, 16, 8172–8180

force on atoms was converged below 0.005 eV·Å^{-1}. A vacuum layer of 15 Å is used perpendicular to the plane of W atoms. To calculate the modulus of monolayer WS_2, a 12.6 Å × 21.0 Å supercell is built; then, the strains are applied and the DFT calculations are performed with 1 × 1 × 1 *k*-mesh; finally, the modulus is fitted from the DFT results (Figure S10a–c). We calculate the generalized stacking fault energy (GSFE) of bilayer WS_2 using the equation

$$\begin{aligned} E_{\mathrm{GSFE}}(u_i, v_i) &= -112.5\ \mathrm{meV} + (10.8\ \mathrm{meV})(\cos(u_i) + \cos(v_i) + \cos(u_i + v_i)) \\ &\quad - (2.1\ \mathrm{meV})(\cos(u_i + 2v_i) + \cos(u_i - v_i) + \cos(2u_i + v_i)) \\ &\quad - (0.165\ \mathrm{meV})(\cos(2u_i) + \cos(2v_i) + \cos(2u_i + 2v_i)) \end{aligned} \quad (1)$$

Here we used a unit cell of AA stacked WS_2 bilayer with 9 × 9 × 1 *k*-mesh; the top layer was shifted along two basis vectors and formed a 9 × 9 stacking mesh in one unit cell (Figure S10d–f).

ASSOCIATED CONTENT

Supporting Information

The Supporting Information is available free of charge at https://pubs.acs.org/doi/10.1021/acsnano.2c01625.

Gate-dependent PL spectra; optical and fluorescence microscope images; electron diffraction patterns; extensive PFM images; stacked bilayer fabricated on Si substrate; calculated transition of the size of moiré pattern; comparative experiment for verifying strain influence; power-dependent PL spectra; relax of moiré superlattice; supplementary DFT results (PDF)

AUTHOR INFORMATION

Corresponding Authors

Chorng Haur Sow − *Department of Physics, National University of Singapore, Singapore 117542; Centre for Advanced 2D Materials, National University of Singapore, Singapore 117546;* orcid.org/0000-0001-6385-3017; Email: physowch@nus.edu.sg

Wanxin Sun − *Bruker Nano Surface Division, The Matrix, Singapore 138671*; Email: wanxin.sun@bruker.com

Feng Ding − *Centre for Multidimensional Carbon Materials, Institute for Basic Science, Ulsan, Korea 44919;* orcid.org/0000-0001-9153-9279; Email: f.ding@unist.ac.kr

Authors

Xinyun Wang − *Department of Physics, National University of Singapore, Singapore 117542; Centre for Advanced 2D Materials, National University of Singapore, Singapore 117546*

Yuzhou Zhao − *Department of Chemistry, University of Wisconsin—Madison, Madison, Wisconsin 53706, United States;* orcid.org/0000-0002-1610-8273

Xiao Kong − *Centre for Multidimensional Carbon Materials, Institute for Basic Science, Ulsan, Korea 44919*

Qi Zhang − *Department of Physics, National University of Singapore, Singapore 117542;* orcid.org/0000-0003-4201-7196

Hong Kuan Ng − *Department of Physics, National University of Singapore, Singapore 117542*

Sharon Xiaodai Lim − *Department of Physics, National University of Singapore, Singapore 117542;* orcid.org/0000-0001-9198-8998

Yue Zheng − *Department of Physics, National University of Singapore, Singapore 117542; Centre for Advanced 2D Materials, National University of Singapore, Singapore 117546*

Xiao Wu − *Department of Chemistry, National University of Singapore, Singapore 117543;* orcid.org/0000-0003-0077-5984

Kenji Watanabe − *Research Center for Functional Materials, National Institute for Materials Science, Namiki Tsukuba, Ibaraki, Japan 305-0044;* orcid.org/0000-0003-3701-8119

Qing-Hua Xu − *Department of Chemistry, National University of Singapore, Singapore 117543;* orcid.org/0000-0002-4153-0767

Takashi Taniguchi − *International Center for Materials Nanoarchitectonics, National Institute for Materials Science, Namiki Tsukuba, Ibaraki, Japan 305-0044;* orcid.org/0000-0002-1467-3105

Goki Eda − *Department of Physics, National University of Singapore, Singapore 117542; Centre for Advanced 2D Materials, National University of Singapore, Singapore 117546; Department of Chemistry, National University of Singapore, Singapore 117543;* orcid.org/0000-0002-1575-8020

Kuan Eng Johnson Goh − *Department of Physics, National University of Singapore, Singapore 117542; Institute of Materials Research and Engineering, A*STAR (Agency for Science, Technology and Research), Singapore 138634; Division of Physics and Applied Physics, School of Physical and Mathematical Sciences, Nanyang Technological University, Singapore 637371;* orcid.org/0000-0003-0599-9696

Song Jin − *Department of Chemistry, University of Wisconsin—Madison, Madison, Wisconsin 53706, United States;* orcid.org/0000-0001-8693-7010

Kian Ping Loh − *Centre for Advanced 2D Materials, National University of Singapore, Singapore 117546; Department of Chemistry, National University of Singapore, Singapore 117543;* orcid.org/0000-0002-1491-743X

Complete contact information is available at: https://pubs.acs.org/10.1021/acsnano.2c01625

Author Contributions

#X. Wang, Y. Zhao, and X. Kong contributed equally to this work. X. Wang conceived the experiments, fabricated the twisted samples, and carried out the PFM characterization and laser modification. Y. Zhao synthesized the WS_2 monolayers. X. Kong performed DFT calculations. X. Wang and Q. Zhang carried out the PL measurements. H. K. Ng and X. Wang carried out the gate-dependent PL measurements. Y. Zheng fabricated the electrodes. X. Wu and X. Wang carried out the lifetime measurements. S. X. Lim performed electron diffraction measurements. X. Wang, Y. Zhao, and X. Kong wrote the manuscript with contributions from all of the authors. C. H. Sow, W. Sun, and F. Ding supervised the entire project.

Notes

The authors declare no competing financial interest.

ACKNOWLEDGMENTS

X. Wang, C. H. Sow, and K. E. J. Goh are grateful for the support from Agency for Science, Technology and Research (A*STAR) under its A*STAR 2D PHAROS Grant 1527000016. K.E.J.G. acknowledges the support from a

Singapore National Research Foundation grant (CRP21-2018-0094) and Agency for Science, Technology and Research (#21709). K. P. Loh acknowledges Tier 3 Grant No. MOE2018-T3-1-005 funded by Singapore's Ministry of Education and Grant No. NRF-CRP22-2019-006 funded by National Research Foundation Competitive Research Program, Prime's Minister Office, Singapore. S. Jin and Y. Zhao acknowledge support by the Department of Energy, Office of Basic Energy Sciences, Division of Materials Science and Engineering, under Award DE-FG02-09ER46664. K. Watanabe and T. Taniguchi acknowledge support from the Elemental Strategy Initiative conducted by the MEXT, Japan, Grant No. JPMXP0112101001 and JSPS KAKENHI Grant No. JP20H00354.

REFERENCES

(1) Cao, Y.; Fatemi, V.; Fang, S.; Watanabe, K.; Taniguchi, T.; Kaxiras, E.; Jarillo-Herrero, P. Unconventional Superconductivity in Magic-Angle Graphene Superlattices. *Nature* **2018**, *556* (7699), 43−50.

(2) Cao, Y.; Fatemi, V.; Demir, A.; Fang, S.; Tomarken, S. L.; Luo, J. Y.; Sanchez-Yamagishi, J. D.; Watanabe, K.; Taniguchi, T.; Kaxiras, E.; Ashoori, R. C.; Jarillo-Herrero, P. Correlated Insulator Behaviour at Half-Filling in Magic-Angle Graphene Superlattices. *Nature* **2018**, *556* (7699), 80−84.

(3) Alexeev, E. M.; Ruiz-Tijerina, D. A.; Danovich, M.; Hamer, M. J.; Terry, D. J.; Nayak, P. K.; Ahn, S.; Pak, S.; Lee, J.; Sohn, J. I.; Molas, M. R.; Koperski, M.; Watanabe, K.; Taniguchi, T.; Novoselov, K. S.; Gorbachev, R. V.; Shin, H. S.; Fal'ko, V. I.; Tartakovskii, A. I. Resonantly Hybridized Excitons in Moiré Superlattices in van der Waals Heterostructures. *Nature* **2019**, *567* (7746), 81−86.

(4) Jin, C.; Regan, E. C.; Yan, A.; Iqbal Bakti Utama, M.; Wang, D.; Zhao, S.; Qin, Y.; Yang, S.; Zheng, Z.; Shi, S.; Watanabe, K.; Taniguchi, T.; Tongay, S.; Zettl, A.; Wang, F. Observation of Moiré Excitons in WSe_2/WS_2 Heterostructure Superlattices. *Nature* **2019**, *567* (7746), 76−80.

(5) Seyler, K. L.; Rivera, P.; Yu, H.; Wilson, N. P.; Ray, E. L.; Mandrus, D. G.; Yan, J.; Yao, W.; Xu, X. Signatures of Moiré-Trapped Valley Excitons in $MoSe_2/WSe_2$ Heterobilayers. *Nature* **2019**, *567* (7746), 66−70.

(6) Tran, K.; Moody, G.; Wu, F.; Lu, X.; Choi, J.; Kim, K.; Rai, A.; Sanchez, D. A.; Quan, J.; Singh, A.; Embley, J.; Zepeda, A.; Campbell, M.; Autry, T.; Taniguchi, T.; Watanabe, K.; Lu, N.; Banerjee, S. K.; Silverman, K. L.; Kim, S.; et al. Evidence for Moiré Excitons in van der Waals Heterostructures. *Nature* **2019**, *567* (7746), 71−75.

(7) Weston, A.; Zou, Y.; Enaldiev, V.; Summerfield, A.; Clark, N.; Zólyomi, V.; Graham, A.; Yelgel, C.; Magorrian, S.; Zhou, M.; Zultak, J.; Hopkinson, D.; Barinov, A.; Bointon, T. H.; Kretinin, A.; Wilson, N. R.; Beton, P. H.; Fal'ko, V. I.; Haigh, S. J.; Gorbachev, R. Atomic Reconstruction in Twisted Bilayers of Transition Metal Dichalcogenides. *Nat. Nanotechnol.* **2020**, *15* (7), 592−597.

(8) Wang, X.; Yasuda, K.; Zhang, Y.; Liu, S.; Watanabe, K.; Taniguchi, T.; Hone, J.; Fu, L.; Jarillo-Herrero, P. Interfacial Ferroelectricity in Rhombohedral-Stacked Bilayer Transition Metal Dichalcogenides. *Nat. Nanotechnol.* **2022**, *17*, 367−371.

(9) Sung, J.; Zhou, Y.; Scuri, G.; Zólyomi, V.; Andersen, T. I.; Yoo, H.; Wild, D. S.; Joe, A. Y.; Gelly, R. J.; Heo, H.; Magorrian, S. J.; Bérubé, D.; Valdivia, A. M. M.; Taniguchi, T.; Watanabe, K.; Lukin, M. D.; Kim, P.; Fal'ko, V. I.; Park, H. Broken Mirror Symmetry in Excitonic Response of Reconstructed Domains in Twisted MoSe2/MoSe2 Bilayers. *Nat. Nanotechnol.* **2020**, *15* (9), 750−754.

(10) Bai, Y.; Zhou, L.; Wang, J.; Wu, W.; McGilly, L. J.; Halbertal, D.; Lo, C. F. B.; Liu, F.; Ardelean, J.; Rivera, P.; Finney, N. R.; Yang, X.-C.; Basov, D. N.; Yao, W.; Xu, X.; Hone, J.; Pasupathy, A. N.; Zhu, X. Y. Excitons in Strain-Induced One-Dimensional Moiré Potentials at Transition Metal Dichalcogenide Heterojunctions. *Nat. Mater.* **2020**, *19* (10), 1068−1073.

(11) Yoo, H.; Engelke, R.; Carr, S.; Fang, S.; Zhang, K.; Cazeaux, P.; Sung, S. H.; Hovden, R.; Tsen, A. W.; Taniguchi, T.; Watanabe, K.; Yi, G.-C.; Kim, M.; Luskin, M.; Tadmor, E. B.; Kaxiras, E.; Kim, P. Atomic and Electronic Reconstruction at the van der Waals Interface in Twisted Bilayer Graphene. *Nat. Mater.* **2019**, *18* (5), 448−453.

(12) Quan, J.; Linhart, L.; Lin, M.-L.; Lee, D.; Zhu, J.; Wang, C.-Y.; Hsu, W.-T.; Choi, J.; Embley, J.; Young, C.; Taniguchi, T.; Watanabe, K.; Shih, C.-K.; Lai, K.; MacDonald, A. H.; Tan, P.-H.; Libisch, F.; Li, X. Phonon Renormalization in Reconstructed MoS2 Moiré Superlattices. *Nat. Mater.* **2021**, *20* (8), 1100−1105.

(13) Zhu, S.; Johnson, H. T. Moiré-Templated Strain Patterning in Transition-Metal Dichalcogenides and Application in Twisted Bilayer MoS2. *Nanoscale* **2018**, *10* (44), 20689−20701.

(14) Halbertal, D.; Finney, N. R.; Sunku, S. S.; Kerelsky, A.; Rubio-Verdú, C.; Shabani, S.; Xian, L.; Carr, S.; Chen, S.; Zhang, C.; et al. Moiré Metrology of Energy Landscapes in van der Waals Heterostructures. *Nat. Commun.* **2021**, *12* (1), 242.

(15) Purdie, D. G.; Pugno, N. M.; Taniguchi, T.; Watanabe, K.; Ferrari, A. C.; Lombardo, A. Cleaning Interfaces in Layered Materials Heterostructures. *Nat. Commun.* **2018**, *9* (1), 5387.

(16) Zhao, Y.; Jin, S. Controllable Water Vapor Assisted Chemical Vapor Transport Synthesis of WS2−MoS2 Heterostructure. *ACS Mater. Lett.* **2020**, *2* (1), 42−48.

(17) Ahn, G. H.; Amani, M.; Rasool, H.; Lien, D.-H.; Mastandrea, J. P.; Ager, J. W., III; Dubey, M.; Chrzan, D. C.; Minor, A. M.; Javey, A. Strain-Engineered Growth of Two-Dimensional Materials. *Nat. Commun.* **2017**, *8* (1), 608.

(18) van der Zande, A. M.; Huang, P. Y.; Chenet, D. A.; Berkelbach, T. C.; You, Y.; Lee, G.-H.; Heinz, T. F.; Reichman, D. R.; Muller, D. A.; Hone, J. C. Grains and Grain Boundaries in Highly Crystalline Monolayer Molybdenum Disulphide. *Nat. Mater.* **2013**, *12* (6), 554−561.

(19) Zhu, D.; Shu, H.; Jiang, F.; Lv, D.; Asokan, V.; Omar, O.; Yuan, J.; Zhang, Z.; Jin, C. Capture the Growth Kinetics of CVD Growth of Two-Dimensional MoS2. *npj 2D Mater. Appl.* **2017**, *1* (1), 8.

(20) Zhao, Y.; Kong, X.; Shearer, M. J.; Ding, F.; Jin, S. Chemical Etching of Screw Dislocated Transition Metal Dichalcogenides. *Nano Lett.* **2021**, *21* (18), 7815−7822.

(21) Pak, S.; Lee, J.; Lee, Y.-W.; Jang, A. R.; Ahn, S.; Ma, K. Y.; Cho, Y.; Hong, J.; Lee, S.; Jeong, H. Y.; Im, H.; Shin, H. S.; Morris, S. M.; Cha, S.; Sohn, J. I.; Kim, J. M. Strain-Mediated Interlayer Coupling Effects on the Excitonic Behaviors in an Epitaxially Grown MoS2/WS2 van der Waals Heterobilayer. *Nano Lett.* **2017**, *17* (9), 5634−5640.

(22) He, X.; Li, H.; Zhu, Z.; Dai, Z.; Yang, Y.; Yang, P.; Zhang, Q.; Li, P.; Schwingenschlogl, U.; Zhang, X. Strain Engineering in Monolayer WS2, MoS2, and the WS2/MoS2 Heterostructure. *Appl. Phys. Lett.* **2016**, *109* (17), 173105.

(23) Deng, S.; Sumant, A. V.; Berry, V. Strain Engineering in Two-Dimensional Nanomaterials Beyond Graphene. *Nano Today* **2018**, *22*, 14−35.

(24) Jauregui, L. A.; Joe, A. Y.; Pistunova, K.; Wild, D. S.; High, A. A.; Zhou, Y.; Scuri, G.; De Greve, K.; Sushko, A.; Yu, C.-H.; Taniguchi, T.; Watanabe, K.; Needleman, D. J.; Lukin, M. D.; Park, H.; Kim, P. Electrical Control of Interlayer Exciton Dynamics in Atomically Thin Heterostructures. *Science* **2019**, *366* (6467), 870−875.

(25) Wang, Z.; Chiu, Y.-H.; Honz, K.; Mak, K. F.; Shan, J. Electrical Tuning of Interlayer Exciton Gases in WSe2 Bilayers. *Nano Lett.* **2018**, *18* (1), 137−143.

(26) McGilly, L. J.; Kerelsky, A.; Finney, N. R.; Shapovalov, K.; Shih, E.-M.; Ghiotto, A.; Zeng, Y.; Moore, S. L.; Wu, W.; Bai, Y.; Watanabe, K.; Taniguchi, T.; Stengel, M.; Zhou, L.; Hone, J.; Zhu, X.; Basov, D. N.; Dean, C.; Dreyer, C. E.; Pasupathy, A. N. Visualization of Moiré Superlattices. *Nat. Nanotechnol.* **2020**, *15* (7), 580−584.

(27) Halbertal, D.; Finney, N. R.; Sunku, S. S. Moiré metrology of energy landscapes in van der Waals heterostructures. *Nat. Commun.* **2021**, *12* (1), 242.

https://doi.org/10.1021/acsnano.2c01625
ACS Nano 2022, 16, 8172−8180

(28) Lee, Y. Y.; Hu, Z.; Wang, X.; Sow, C.-H. Progressive Micromodulation of Interlayer Coupling in Stacked WS2/WSe2 Heterobilayers Tailored by a Focused Laser Beam. *ACS Appl. Mater. Interfaces* **2018**, *10* (43), 37396−37406.
(29) Kumar, P.; Liu, J.; Motlag, M.; Tong, L.; Hu, Y.; Huang, X.; Bandopadhyay, A.; Pati, S. K.; Ye, L.; Irudayaraj, J.; Cheng, G. J. Laser Shock Tuning Dynamic Interlayer Coupling in Graphene−Boron Nitride Moiré Superlattices. *Nano Lett.* **2019**, *19* (1), 283−291.
(30) Venkatakrishnan, A.; Chua, H.; Tan, P.; Hu, Z.; Liu, H.; Liu, Y.; Carvalho, A.; Lu, J.; Sow, C. H. Microsteganography on WS2Monolayers Tailored by Direct Laser Painting. *ACS Nano* **2017**, *11* (1), 713−720.
(31) Castellanos-Gomez, A.; Barkelid, M.; Goossens, A. M.; Calado, V. E.; van der Zant, H. S. J.; Steele, G. A. Laser-Thinning of MoS2: On Demand Generation of a Single-Layer Semiconductor. *Nano Lett.* **2012**, *12* (6), 3187−3192.
(32) Wang, D.; Chen, G.; Li, C.; Cheng, M.; Yang, W.; Wu, S.; Xie, G.; Zhang, J.; Zhao, J.; Lu, X.; Chen, P.; Wang, G.; Meng, J.; Tang, J.; Yang, R.; He, C.; Liu, D.; Shi, D.; Watanabe, K.; Taniguchi, T.; et al. Thermally Induced Graphene Rotation on Hexagonal Boron Nitride. *Phys. Rev. Lett.* **2016**, *116* (12), 126101.
(33) Hui, Y. Y.; Liu, X.; Jie, W.; Chan, N. Y.; Hao, J.; Hsu, Y.-T.; Li, L.-J.; Guo, W.; Lau, S. P. Exceptional Tunability of Band Energy in a Compressively Strained Trilayer MoS2 Sheet. *ACS Nano* **2013**, *7* (8), 7126−7131.
(34) Yu, Y.; Yu, Y.; Xu, C.; Cai, Y.-Q.; Su, L.; Zhang, Y.; Zhang, Y.-W.; Gundogdu, K.; Cao, L. Engineering Substrate Interactions for High Luminescence Efficiency of Transition-Metal Dichalcogenide Monolayers. *Adv. Funct. Mater.* **2016**, *26* (26), 4733−4739.
(35) Liu, H.; Wang, C.; Liu, D.; Luo, J. Neutral and Defect-Induced Exciton Annihilation in Defective Monolayer WS2. *Nanoscale* **2019**, *11* (16), 7913−7920.
(36) Carozo, V.; Wang, Y.; Fujisawa, K.; Carvalho, B. R.; McCreary, A.; Feng, S.; Lin, Z.; Zhou, C.; Perea-López, N.; Elías, A. L.; Kabius, B.; Crespi, V. H.; Terrones, M. Optical Identification of Sulfur Vacancies: Bound Excitons at the Edges of Monolayer Tungsten Disulfide. *Sci. Adv.* **2017**, *3* (4), e1602813.
(37) Lin, Z.; Carvalho, B. R.; Kahn, E.; Lv, R.; Rao, R.; Terrones, H.; Pimenta, M. A.; Terrones, M. Defect Engineering of Two-Dimensional Transition Metal Dichalcogenides. *2D Mater.* **2016**, *3* (2), 022002.
(38) Tongay, S.; Suh, J.; Ataca, C.; Fan, W.; Luce, A.; Kang, J. S.; Liu, J.; Ko, C.; Raghunathanan, R.; Zhou, J.; Ogletree, F.; Li, J.; Grossman, J. C.; Wu, J. Defects Activated Photoluminescence in Two-Dimensional Semiconductors: Interplay between Bound, Charged and Free Excitons. *Sci. Rep.* **2013**, *3* (1), 2657.
(39) Zhao, X.; Dan, J.; Chen, J.; Ding, Z.; Zhou, W.; Loh, K. P.; Pennycook, S. J. Atom-by-Atom Fabrication of Monolayer Molybdenum Membranes. *Adv. Mater.* **2018**, *30* (23), 1707281.
(40) Jeong, H. Y.; Jin, Y.; Yun, S. J.; Zhao, J.; Baik, J.; Keum, D. H.; Lee, H. S.; Lee, Y. H. Heterogeneous Defect Domains in Single-Crystalline Hexagonal WS2. *Adv. Mater.* **2017**, *29* (15), 1605043.
(41) Chu, Z.; Wang, C.-Y.; Quan, J.; Zhang, C.; Lei, C.; Han, A.; Ma, X.; Tang, H.-L.; Abeysinghe, D.; Staab, M.; Zhang, X.; MacDonald, A. H.; Tung, V.; Li, X.; Shih, C.-K.; Lai, K. Unveiling Defect-Mediated Carrier Dynamics in Monolayer Semiconductors by Spatiotemporal Microwave Imaging. *Proc. Nat. Acad. Sci.* **2020**, *117* (25), 13908.

https://doi.org/10.1021/acsnano.2c01625
ACS Nano 2022, 16, 8172−8180